nature neuroscience

Neurons in monkey visual area V2 encode combinations of orientations

Akiyuki Anzai[1,2], Xinmiao Peng[1,2] & David C Van Essen[1]

Contours and textures are important attributes of object surfaces, and are often described by combinations of local orientations in visual images. To elucidate the neural mechanisms underlying contour and texture processing, we examined receptive field (RF) structures of neurons in visual area V2 of the macaque monkey for encoding combinations of orientations. By measuring orientation tuning at several locations within the classical RF, we found that a majority (70%) of V2 neurons have similar orientation tuning throughout the RF. However, many others have RFs containing subregions tuned to different orientations, most commonly about 90° apart. By measuring interactions between two positions within the RF, we found that approximately one-third of neurons show inhibitory interactions that make them selective for combinations of orientations. These results indicate that V2 neurons could play an important role in analyzing contours and textures and could provide useful cues for surface segmentation.

Natural images typically contain oriented segments associated with contours and textures of object surfaces. Therefore, it is useful for the visual system to analyze orientations in local regions and determine their spatial relationships, not only for representing contours and textures but also for segmenting surfaces to segregate figures from the background.

The analysis of orientation begins in the primary visual cortex (V1), where orientation selectivity emerges in individual neurons[1,2]. Adjacent area V2 receives massive projections from V1 (refs. 3,4), and it too contains many orientation selective neurons[5,6]. As RFs of V2 neurons are on average a few times larger in diameter than those of V1 neurons for a given eccentricity[7], each V2 neuron presumably receives inputs from several V1 neurons with slightly different RF positions. This raises a question as to whether converging V1 inputs are tuned to similar or different orientations.

Studies using sinusoidal gratings[8] or single bars[9] reported V2 orientation selectivity similar to that found in V1, consistent with V2 neurons receiving V1 inputs of like orientation preferences. On the other hand, many V2 neurons respond better to complex stimuli such as angles, curves, and noncartesian gratings than to conventional stimuli such as bars and sinusoidal gratings[10–12]. Such properties might arise from RF mechanisms that combine V1 inputs of different orientation preferences. To reconcile the difference between these results requires determining V2 RF organization.

Here we examine RF structure of V2 neurons in anesthetized, paralyzed macaque monkeys, using oriented patches much smaller than the RF. We show that neurons in V2 show two types of RF structure: one that is uniform with respect to orientation preference and another that consists of subregions tuned to different orientations. We also report that many V2 neurons of both types show inhibitory interactions within the RF so that they are selective for combinations of orientations. These findings have important implications regarding the neural circuitry underlying orientation analysis in extrastriate visual cortex.

RESULTS

For each neuron, we measured orientation tuning at multiple locations in and around the classical RF and obtained a spatial map of orientation tuning (space-orientation RF). In a subset of neurons, we also measured responses to pairs of gratings at various combinations of orientations and selected positions within the RF to obtain a response map of orientation interactions. Data were acquired from 180 cells with good single-unit isolation and signal-to-noise ratio (S/N) for orientation tuning, orientation interaction or both. Based on histological reconstructions, 136 cells were assigned to V2, 26 to V1, and 18 to V3. We excluded simple cells from our analyses for the reason described in Methods. We first describe space-orientation RFs obtained from the remaining 118 V2 cells, 22 V1 cells, and 18 V3 cells.

Space-orientation RFs in early visual cortical areas

Examples of space-orientation RFs (**Fig. 1**) represent the diversity we encountered. For most V2 neurons examined, orientation tuning was uniform across the RF (**Fig. 1a**). Tuning curves were unimodal and peaked at similar orientations throughout the RF. The preferred orientation varied from cell to cell and collectively spanned the entire range of orientations.

In many others, the orientation tuning was nonuniform. The RF shown in **Figure 1b** contained two segregated regions, one preferring ~80° and the other preferring ~170°, in an L-shaped configuration.

[1]Department of Anatomy and Neurobiology, Washington University School of Medicine, 660 South Euclid Avenue, St. Louis, Missouri 63110, USA. [2]Present addresses: Center for Visual Science, University of Rochester, Meliora Hall 248, Rochester, New York 14627, USA (A.A.) and Department of Neurobiology and Anatomy, University of Texas-Houston Health Science Center, 6431 Fannin Street, Houston, Texas 77030, USA (X.P.). Correspondence should be addressed to A.A. (aanzai@cvs.rochester.edu).

Received 27 April; accepted 14 August; published online 16 September 2007; doi:10.1038/nn1975

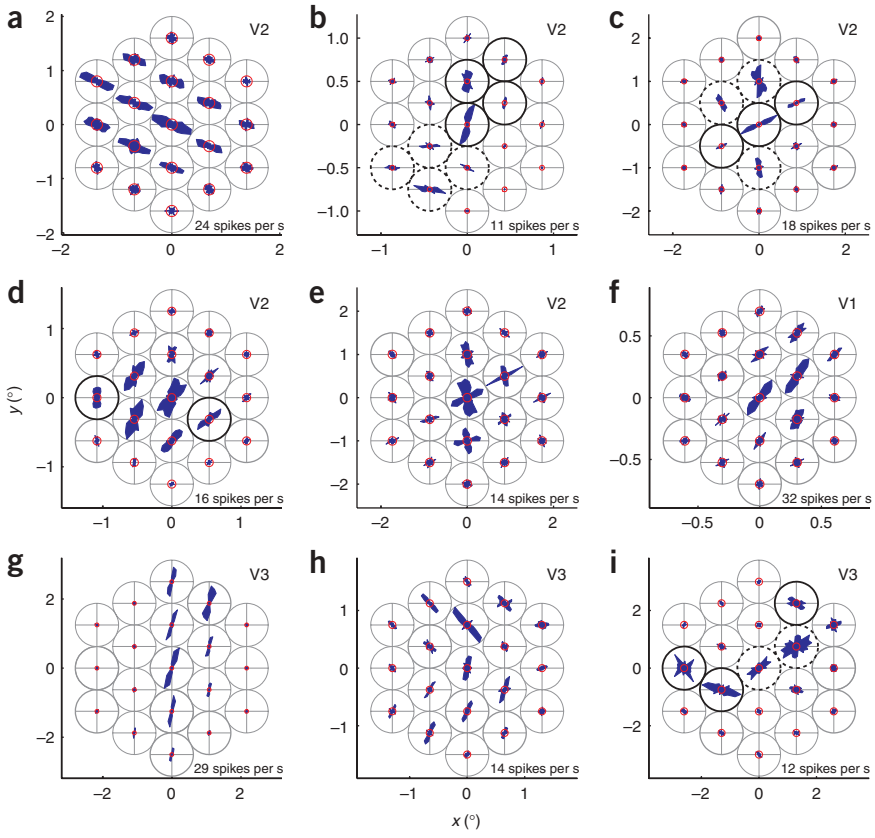

Figure 1 Examples of space-orientation RF maps for neurons in early visual cortical areas. Responses (filled blue curves) of neurons relative to the baseline (mean) firing rates (red circles) are plotted in polar coordinate as a function of stimulus orientation at 19 positions arranged in hexagonal arrays in space (*x* and *y*). Gray circles, locations and the size of stimulus patches used to obtain orientation tuning. Value in spikes per second at the lower right corner of each map indicates maximum firing rate as represented by the radius of the gray circle at each location. Orientation increases counterclockwise from 0° at the 3 o'clock position on each gray circle. Results for the orientation range between 0° and 180° were repeated to complete the polar plot in full circle. Solid and dashed black circles, subregions tuned to different orientations. (**a**–**e**) Maps from V2 neurons with uniform (**a**) and nonuniform (**b**–**e**) RF structures. (**f**) Map from a V1 neuron. (**g**–**i**) Maps from V3 neurons with uniform (**g**) and nonuniform (**h**,**i**) RF structures.

Another RF (**Fig. 1c**) consisted of a central region tuned to ~25° flanked by two regions tuned to ~110°.

Some nonuniform RFs showed more moderate and gradual shifts in preferred orientation. For instance, the preferred orientation of the RF shown in **Figure 1d** shifted gradually from about 40° on one side of the RF to 90° on the other.

We also encountered RFs with bimodal tuning (**Fig. 1e**). Apparent bimodal tuning might arise if the stimulus patch fell on the border between two segregated regions of unimodal tuning. However, that was unlikely to account for the RF in **Figure 1e** because bimodal tuning locations were not necessarily in between unimodal tuning regions. As preferred orientations of unimodal tuning locations generally matched with peak orientations of bimodal tuning, bimodal tuning was likely to be the result of spatially overlapping excitatory inputs tuned to different orientations.

In V1, neurons showed minimal variations in orientation tuning across the RF. The largest maximum difference in preferred orientation between pairwise locations within the RF we encountered in V1 was 30° (**Fig. 1f**).

As in V2, RFs of most V3 neurons were uniform (**Fig. 1g**) but others were nonuniform (**Fig. 1h**,**i**). Nonuniform RFs of some V3 neurons appeared to have contour-like structure; the RF shown in **Figure 1i** included two regions tuned to orientations around 150° that were separated by another region tuned to around 40° in a U-shaped configuration.

Variations in preferred orientation across the RF

To characterize various RFs quantitatively, we identified locations having S/N exceeding 2 and conducted modality tests[13] to determine the number of modes in the tuning at each location. No tuning curve showed more than two significant peaks. We then fitted to each tuning curve a von Mises function[14] or a sum of two von Mises functions, depending on the number of modes, to estimate the preferred orientation(s).

Distributions of preferred orientations are shown in **Figure 2.** A scatter plot of preferred orientations for two locations that had the largest orientation difference within each V2 RF (**Fig. 2a**) showed data points mostly scattered along the unity line, indicating that most V2 neurons had only small differences in preferred orientation within their RFs. However, some neurons showed orientation differences near ±90°. This is more evident in the histogram of differences in preferred orientation (**Fig. 2b**), which was bimodal (test for unimodality, $P < 0.01$; test for bimodality, $P > 0.99$). Although the largest difference among randomly (uniformly) distributed orientation preferences is expected to be ±90°, that was not the reason for the cluster around ±90°. A scatter plot of all pairwise combinations of preferred orientations within each V2 RF having a maximum orientation difference exceeding ±30° (**Fig. 2e**) showed data points still concentrated around 0 and ±90° rather than being random. This was confirmed by the histogram of orientation differences (**Fig. 2f**), which was bimodal (test for unimodality, $P < 0.01$; test for bimodality, $P > 0.99$) with peaks around 0° and ±90°. That is, if a pair of locations within an RF is chosen randomly from our sample, the difference in preferred orientations between the two locations is most likely to be around either 0° or ±90°.

These results indicate that orientation selective V2 neurons can be divided into two groups: one with uniform RF structure and another with nonuniform structure. Of the 100 V2 RFs included in this analysis (excluding 18 RFs with poor fits), we classified 70 (70%) as having uniform RFs because they showed at most a ±30° difference in preferred orientation, and the remaining 30 (30%) we classified as nonuniform. We subjectively classified approximately one-third (11) of nonuniform RFs as bipartite (two subregions), another one-third (9) as containing bimodally tuned regions, one-sixth (5) as tripartite, and one-tenth (3) as having a gradual change in preferred orientation; two nonuniform RFs were unclassified.

We also found nonuniform RFs in 7 of 18 (39%) V3 neurons. The scatter plot and the histogram of largest differences in preferred orientation within the RF for V3 neurons (**Fig. 2c**,**d**) were qualitatively

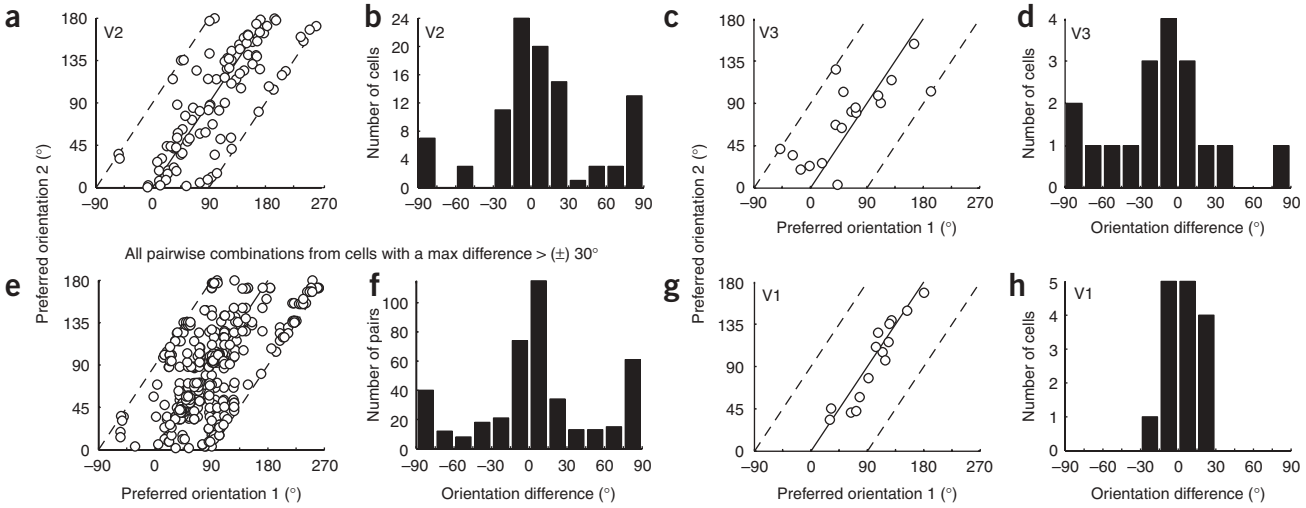

Figure 2 Distributions of preferred orientations between pairwise locations within the RF. (**a**–**h**) Scatter plots of preferred orientations and histograms of differences between the preferred orientations. Preferred orientations from a bimodal tuning curve were treated as if each belonged to a unimodal tuning curve at a different location. (**a**,**c**,**g**) Scatter plots of pairs of preferred orientations representing the largest difference found in each RF. Solid and dashed lines, loci corresponding to orientation differences of 0° and ± 90°, respectively. Preferred orientations with standard errors greater than 9° were excluded (see Methods); remaining data for V2 neurons ($N = 100$) are shown in **a**, along with those for V3 ($N = 18$) in **c** and V1 ($N = 15$) in **g** for comparison. (**b**,**d**,**h**) Histograms of maximum differences in preferred orientation for V2 (**b**), V3 (**d**), and V1 (**h**). (**e**) Scatter plot of all pairwise combinations of preferred orientations within each RF for V2 cells with the maximum orientation difference exceeding ±30° ($N = 424$). (**f**) A histogram of orientation differences for the data shown in **e**.

similar to those for V2 neurons (**Fig. 2a**,**b**), although the V3 histogram was not significantly bimodal (test for unimodality, $P > 0.97$). Histograms generated by randomly sampling from the V2 histogram so that its sample size matched that of the V3 histogram were bimodal in only 22 of 1,000 bootstrap simulations; this implies that our V3 sample size is not large enough for the modality test to reveal statistical significance in bimodality even if the incidence of nonuniform RFs in V3 were comparable to that in V2.

In contrast, differences in preferred orientation between pairwise locations within the RF for all V1 neurons were limited to ±30° (**Fig. 2g**). The histogram of largest differences in preferred orientation (**Fig. 2h**) was unimodal (test for unimodality, $P > 0.98$), consistent with that of a homogeneous population. It is possible that nonuniform RFs are present in V1 but were missed because our sample size was small. Although we cannot exclude this possibility, we can estimate its likelihood. We randomly sampled cells from the V2 distribution in **Figure 2b** so that its sample size matched that of our V1 sample, and determined that the probability of observing no cells with nonuniform RFs would be 0.005 (based on 10^5 bootstrap simulations). In other words, had V1 contained cells with nonuniform RFs in the proportion similar to that found in V2, it would be very rare to find only uniform RFs. As already noted, we found nonuniform RFs in V3 even though the V3 sample size was similar to that of V1. Therefore, the proportion of V1 neurons with nonuniform RFs, if they exist at all, is likely to be much smaller than those in V2 and V3. Consistent with this conclusion, a bayesian estimate[15] for the prevalence of nonuniform RFs in V1 is less than 6%.

Orientation interactions between two positions in the RF

To better understand the computations performed by V2 neurons, it is important to know how inputs from different parts of the RF are combined. Of particular interest are interactions that facilitate neuronal responses to certain combinations of orientations but suppress them for others. We now describe results of double-patch interaction measurements obtained from 94 position pairs (188 directional interactions) with good S/Ns in 31 V2 neurons.

In an exemplar neuron (**Fig. 3**), the space-orientation RF (**Fig. 3a**) was classified as uniform. We selected positions 5 and 8 for the subsequent orientation interaction measurement. A map of responses to pairs of stimuli presented at the chosen positions as a function of stimulus orientation (**Fig. 3b**) showed that responses peaked around the preferred orientation (40°) of the stimulus positions and were mostly confined to a narrow range of orientations.

One way to assess spatial summation within the RF is to compare orientation tuning measured with single-patch stimuli to that measured with double-patch stimuli of the same orientation to examine the effect of doubling the stimulus area on the orientation tuning. Single-patch orientation tuning for individual positions and double-patch orientation tuning (**Fig. 3c**) extracted from the map in **Figure 3b** along the main diagonal all peaked around the same orientation, but the amplitude of the double-patch tuning curve was almost three times that of the single-patch tuning curves. This indicates that the spatial summation between the two positions was facilitatory when the cell was stimulated at the preferred orientation.

Another way to characterize RF spatial summation is to compare shapes of orientation tuning curves measured at one (testing) position while the stimulus orientation at another (conditioning) position was either optimal (the orientation at the response peak; optimal conditioning) or orthogonal to the optimal (orthogonal conditioning). Before describing results of this analysis, let us consider the four conceptually distinct possibilities (schematized in **Fig. 3d**–**g**). (i) The orientation tuning curves for optimal and orthogonal conditioning may be shifted vertically from each other but their shapes remain unchanged (**Fig. 3d**). This would indicate that the inputs from the conditioning position had an additive or subtractive influence on the response of a V2 neuron (linear summation), with the vertical shift corresponding to the difference in the amount of excitation elicited by the two conditioning stimuli. (ii) In addition to the vertical shift, the tuning for orthogonal conditioning may have reduced amplitude compared to that for optimal conditioning (**Fig. 3e**). This would suggest that the inputs from the conditioning position had a multiplicative or divisive effect on the

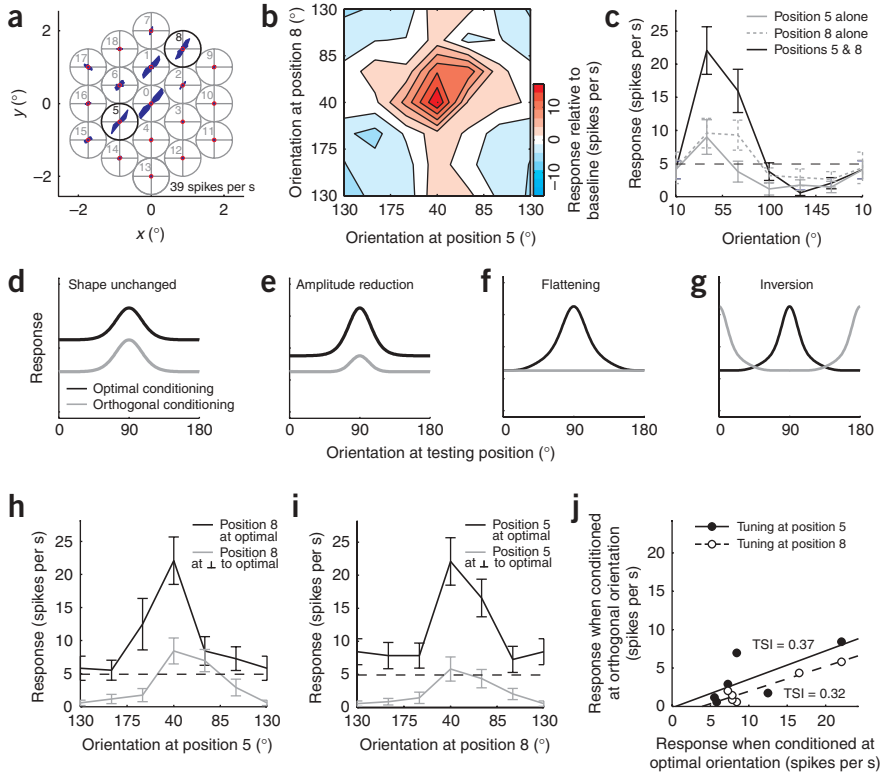

Figure 3 Orientation interaction results from an exemplar V2 neuron with a uniform RF. (**a**) A space-orientation RF obtained just before an orientation interaction measurement. Conventions as in **Figure 1**. Stimulus positions are numbered inside gray circles. Black circles, the two positions for which interactions are shown in **b**. (**b**) A response map of orientation interactions between two positions tuned to similar orientations. The map has been shifted so that its peak (estimated in a gaussian-filtered map) appears at the center. (**c**) Single-patch (solid and dashed gray lines) and double-patch (black line) orientation tuning curves. Dashed black line, baseline firing rate; error bars, ± s.e.m. (**d**–**g**) Schematic orientation tuning for optimal (black line) and orthogonal (gray line) conditioning in four possibilities: no change in tuning shape (**d**), amplitude reduction (**e**), flattening (**f**) and inversion (**g**). (**h**) Orientation tuning curves at position 5 with optimal (black line) and orthogonal (gray line) conditioning at position 8. Error bars, ± s.e.m. (**i**) Orientation tuning curves at position 8 with a conditioning stimulus at position 5. (**j**) Relationship between tuning curves for optimal and orthogonal conditioning. Responses of the tuning curve for orthogonal conditioning are plotted against those for optimal conditioning. Filled and open circles, data from **h** and **i**, respectively. Solid and dashed lines, regression lines to the filled and open circles, which had slope (TSI) values of 0.37 and 0.32, respectively.

response of a V2 neuron (linear or nonlinear scaling). The simplest mechanism that can account for such a process would be an expansive output nonlinearity such as half-squaring[16] after a linear summation stage. (iii) The tuning for orthogonal conditioning may become flat (**Fig. 3f**). This process would require an inhibitory mechanism tuned for orientation (orientation tuned inhibition). (iv) The tuning for orthogonal conditioning may have an inverted shape of the tuning for optimal conditioning (**Fig. 3g**). This would signify that inhibition for orthogonal conditioning decreased depending on the orientation of the testing stimulus: that is, a removal of inhibition (disinhibition). We encountered evidence for each of these mechanisms in the population of V2 neurons studied.

Returning to the preceding exemplar neuron, **Figure 3h** shows orientation tuning curves at position 5 extracted from **Figure 3b** while keeping the orientation at position 8 either at optimal or at orthogonal to optimal, where the optimal orientation is defined by the stimulus orientation of a given position at the response peak. Similarly, **Figure 3i** shows tuning curves at position 8, with position 5 serving as the conditioning position. In both panels, the tuning curve for orthogonal conditioning was shifted downward and reduced in

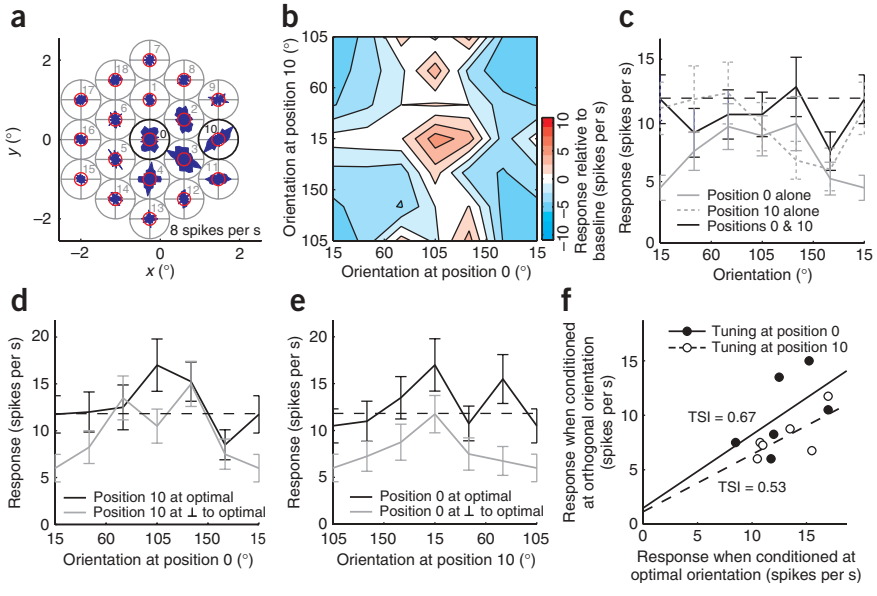

Figure 4 Orientation interaction results from a V2 neuron with a nonuniform RF. (**a**) A space-orientation RF obtained just before an orientation interaction measurement. Conventions as in **Figures 1** and **3**. Black circles, the two positions for which orientation interactions are shown in **b**. (**b**) A response map of orientation interactions between two positions tuned to different orientations. The map has been shifted so that its peak appears at the center. (**c**) Single-patch and double-patch orientation tuning curves. Conventions as in **Figure 3c**. (**d**) Orientation tuning curves at position 0, conditioned at position 10. Conventions as in **Figure 3h**. (**e**) Orientation tuning curves at position 10 conditioned at position 0. Conventions as in **Figure 3i**. (**f**) A relationship between tuning curves for optimal and orthogonal conditioning, plotted as in **Figure 3j**. Filled and open circles, data from **d** and **e**, respectively. Solid and dashed lines, regression lines to the filled and open circles with slope (TSI) values of 0.67 and 0.53, respectively.

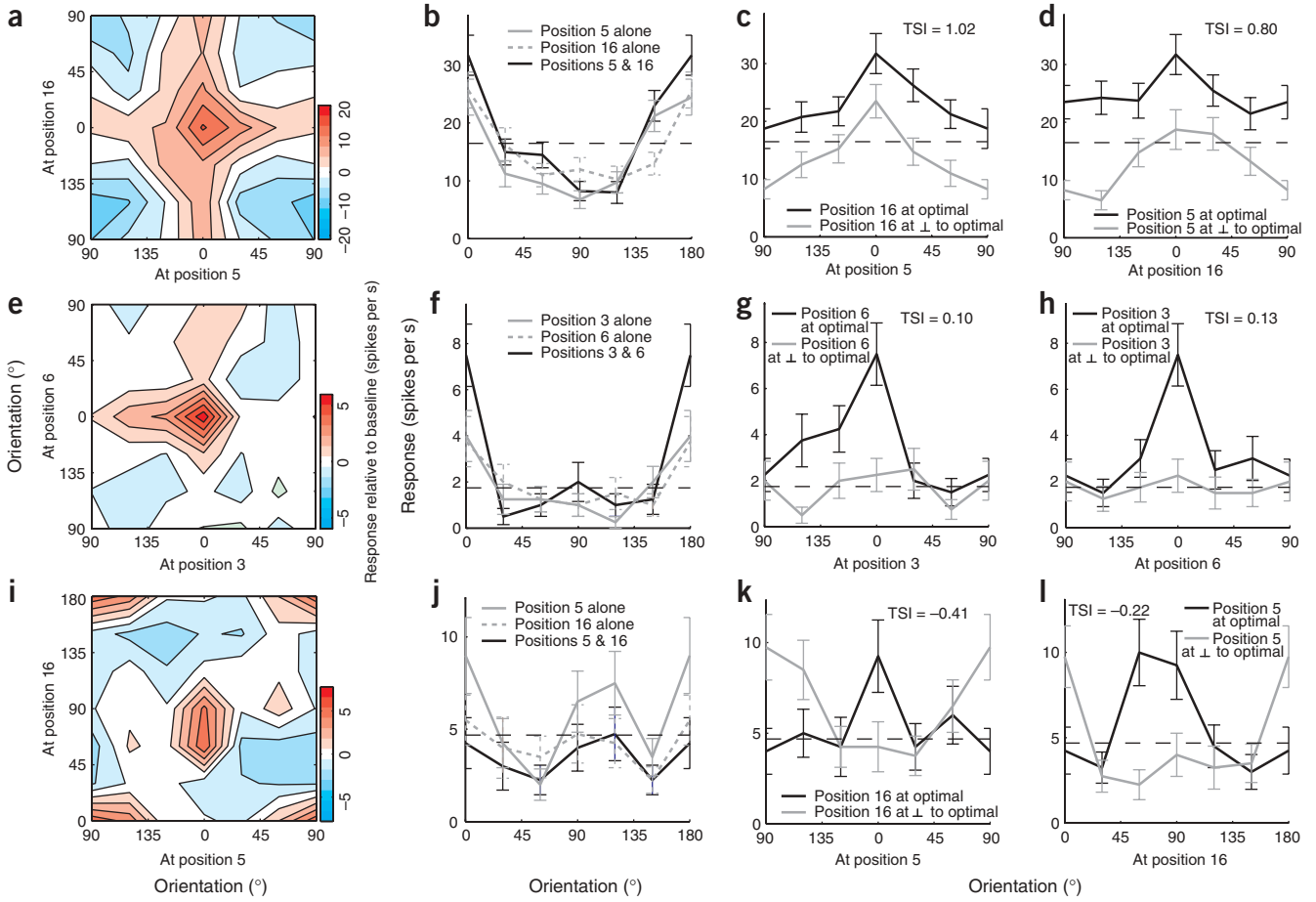

Figure 5 Further examples of orientation interaction results. (**a**–**d**) From a neuron that showed no change of tuning shape for orthogonal conditioning. (**e**–**h**) From a neuron that showed flattening. (**i**–**l**) From a neuron that showed inversion. (**a**,**e**,**i**) Orientation interaction maps. Conventions as in **Figure 3b**. (**b**,**f**,**j**) Single-patch and double-patch orientation tuning curves. Conventions as in **Figure 3c**. (**c**,**d**,**g**,**h**,**k**,**l**) Orientation tuning curves for one position with a conditioning stimulus at another position. Conventions as in **Figure 3h**.

amplitude, compared to that for optimal conditioning. This corresponds to an amplitude reduction case (**Fig. 3e**).

To quantify the degree of change in tuning shape, we plotted responses for orthogonal conditioning against those for optimal conditioning (**Fig. 3j**) and fitted the plot with a regression line. If the tuning shape remained unchanged (**Fig. 3d**), the slope of the regression line would be close to unity. The slope would be positive but less than unity for amplitude reduction (**Fig. 3e**), near zero for flattening of tuning (**Fig. 3f**), and negative for tuning inversion (**Fig. 3g**). We take the slope as an objective measure of similarity between tuning shapes for optimal and orthogonal conditioning, and call it a tuning similarity index (TSI). In **Figure 3j**, TSIs were 0.37 and 0.32 for positions 5 and 8, respectively, consistent with the amplitude reduction scheme (**Fig. 3e**).

Another exemplar neuron had a nonuniform RF (**Fig. 4a**) that included one location (position 0) preferring vertical (90°) and another (position 10) preferring 30°. The map of orientation interactions between these positions showed a peak approximately at the preferred orientations of the positions (**Fig. 4b**).

Unlike the neuron in **Figure 3c**, the double-patch tuning of this neuron was relatively flat (**Fig. 4c**). This is not surprising because the tuning was taken from **Figure 4b** along the locus of equal orientations, which lies along off-diagonals (not the main diagonal through the response peak). The double-patch tuning does not appear to be a simple sum of the two single-patch tuning curves, suggesting that little summation, and perhaps even suppression, occurred between the two positions when the cell was stimulated with the same orientation.

The shape differences between tuning curves for optimal and orthogonal conditioning shown in **Figure 4d**,**e** are qualitatively similar to those in **Figure 3h**,**i**, and yielded TSIs of 0.67 and 0.53 for positions 0 and 10, respectively (**Fig. 4f**). Therefore, the effect of orthogonal conditioning on this cell was a reduction in net excitation with a slight scaling (**Fig. 3e**).

Examples of cells representing the remaining three types of interactions (**Fig. 3d**,**f**,**g**) include one whose interaction map (**Fig. 5a**) showed a cross-like response pattern that extended along the vertical and horizontal axes through the peak. The amplitude of the double-patch tuning obtained from this map was about 50% larger than those of single-patch tuning curves (**Fig. 5b**), indicating partial summation. The tuning curves for optimal and orthogonal conditioning had similar shapes (**Fig. 5c**,**d**) with TSIs close to unity, consistent with linear summation (**Fig. 3d**).

In contrast, the map in **Figure 5e** showed no pronounced cross-like pattern. The peak amplitude of the double-patch tuning (**Fig. 5f**) was approximately twice that of either single-patch tuning curve, indicating complete summation when the same orientation was presented to the

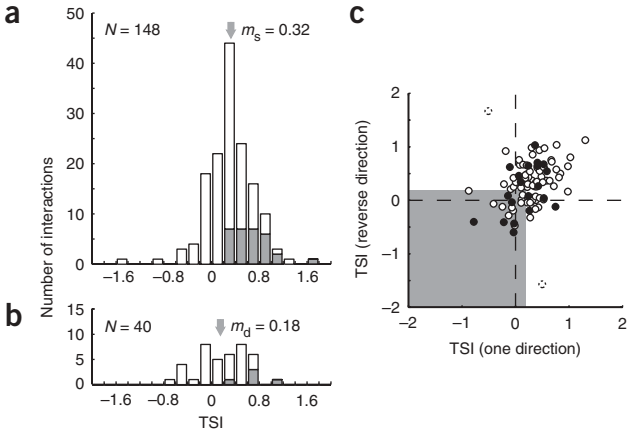

Figure 6 Distributions of TSIs. (**a**,**b**) Histograms of TSIs. Gray bars, TSIs that are statistically significantly greater than 0 ($P < 0.05$). Arrows, means of the distributions. (**a**) TSI histogram for interactions between positions whose single-patch orientation tuning curves peaked at similar orientations ($\leq 30°$). Mean $m_s = 0.32$ ($N = 142$). (**b**) TSI histogram for interactions between positions whose single-patch orientation tuning curves peaked at dissimilar orientations ($>30°$). Mean $m_d = 0.18$ ($N = 46$), which is statistically smaller than m_s, one-tailed t-test, $P = 0.022$. (**c**) Scatter plot of TSIs for the two directions of interaction. For each pair of positions, a TSI for one direction of interaction is plotted against that for the reverse direction by randomly assigning one direction to the x axis and the other to the y axis. Open and filled circles, position pairs tuned to similar and dissimilar orientations, respectively; dashed circles, outliers whose deviations from the regression line fit to the data are outside their 95% confidence intervals. Shaded area, a region of TSIs < 0.2.

two interacting positions. Tuning curves for orthogonal conditioning (**Fig. 5g**,**h**) were virtually flat (**Fig. 3f**), resulting in low TSIs (0.10 and 0.13) and implicating an inhibitory mechanism tuned for orientation.

In contrast to the interaction maps with a single peak described above, some maps had response peaks at the four corners as well as the center. One example (**Fig. 5i**) was obtained for two positions having bimodal orientation tuning (**Fig. 5j**). The map shows responses to orientation combinations of [0°,90°] and [90°,0°] but not to [0°,0°] and [90°,90°]. The unresponsiveness to uniform orientations is also apparent in the double-patch tuning (**Fig. 5j**). The amplitude of the double-patch tuning is smaller than those of the single-patch tunings, suggesting an inhibitory interaction between the two positions when the stimuli had equal orientations. The tuning curves for optimal and orthogonal conditioning (**Fig. 5k**,**l**) showed shape inversion (**Fig. 3g**) and negative TSIs (–0.41 and –0.22), indicating that inhibition for orthogonal conditioning could be removed depending on the orientation of the testing stimulus.

Inhibitory interactions to encode orientation combinations

To summarize the orientation interaction results, we plotted histograms of TSIs (**Fig. 6a**,**b**) for interactions between positions with, respectively, similar ($\leq 30°$) and dissimilar ($>30°$) orientation preferences in single-patch tuning. Means of the distributions are 0.32 (similar) and 0.18 (dissimilar) (**Fig. 6a**,**b**, respectively); their difference is significant (one-tailed t-test, $P = 0.022$). No TSIs smaller than 0.2 were statistically significantly greater than 0, so we consider TSIs less than 0.2 to indicate either flat or inverted tuning reflecting inhibitory interactions. Based on this criterion, approximately one-third (49/148) of the interactions examined between positions tuned to similar orientations were inhibitory, whereas almost half (19/40) of those between positions tuned to dissimilar orientations were inhibitory. The latter proportion is slightly larger than the former (one-tailed two-sample Z-test, $P < 0.05$), indicating that an inhibitory interaction may be more common among position pairs tuned to dissimilar orientations. Overall, inhibitory interactions were found for at least one position pair in 27 of 31 cells tested.

For each pair of positions, interactions can be examined in two directions: from one position to the other and vice versa. Does the nature of interaction depend on the direction? If one position exerted an inhibitory effect on the other, then the position providing the inhibition would act as a 'gatekeeper' (or on-off switch) for the incoming signal at the other position. If an inhibitory effect were present in mutual directions, then each position would act as a 'gatekeeper' for the other, effectively performing something akin to a logical AND operation signaling a conjunction of inputs.

A scatter plot of TSIs for one direction versus reverse direction (**Fig. 6c**) shows data points that are mostly scattered diagonally except for two outliers, and there is a modest but significant correlation ($r = 0.26$, $P = 0.01$; $r = 0.44$, $P < 0.0001$ without outliers). Therefore, for a given position pair, the nature of interaction is generally similar in the two directions. The shaded area, which indicates a region of TSIs less than 0.2 in both directions, includes 16 data points from 11 of 31 cells examined. In other words, approximately one-third of V2 neurons tested responded to a combination of optimal orientations, but were inhibited when either of the two orientations was set orthogonal to its optimal. These neurons, thus, encode combinations of optimal orientations (see Discussion).

Finally, we tested whether interactions within the same RF are similar compared to those across different RFs. The distribution of TSIs relative to their mean for each RF (within-RF condition) was compared with that generated by randomly selecting samples from a pool of TSIs for all RFs and assigning them to each RF (across-RF condition). The probability that the variance of the distribution in the within-RF condition exceeded that in the across-RF condition was 0.0012 (based on 10^4 bootstrap simulations). Therefore, TSIs within the RF are more similar than those across different RFs, indicating that the nature of interactions does not vary markedly within the RF.

DISCUSSION

To understand computations performed by individual neurons and their functional roles in visual processing, it is essential to study RF structure. However, previous studies of V2 neurons focused on characterizing their responses to various visual patterns rather than RF structure[8–12]. By limiting the scope of analysis to orientation and using small stimulus patches, we examined V2 RF structure and found that orientation-selective excitatory inputs to V2 neurons can be either uniform or nonuniform with respect to orientation preference. Furthermore, we found that the manners in which the excitatory inputs are combined across the RF can be described by a few processes: excitatory, inhibitory and disinhibitory interactions.

In particular, inhibitory and disinhibitory interactions are important because they allow V2 neurons to encode combinations of orientations. (In our terminology, the assertion that V2 neurons 'encode' orientation combinations is not obviated by the fact that the neurons in our study also responded to single patch stimuli in isolation. This is in the same spirit as the more common assertion that many binocular neurons in V1 encode binocular disparity, by virtue of tuning curves that are not flat, despite the fact that most of them also respond to monocular stimulation[17].) When the optimal combination of orientations for a neuron is a particular pair of like orientations, the neuron would show

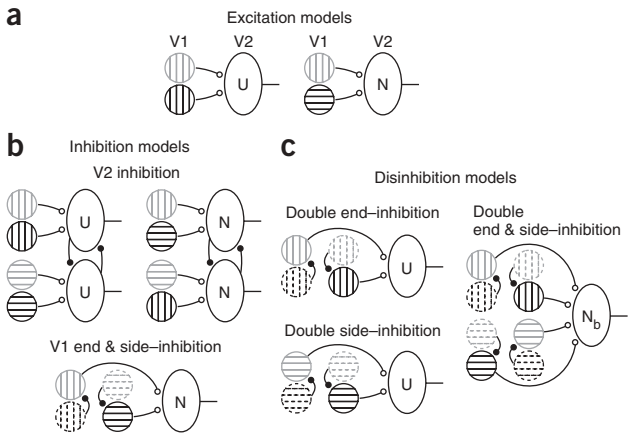

Figure 7 Hypothetical neural circuitries underlying orientation selective V2 RFs. Ellipses, RFs of V2 neurons; letters U, N, and N_b, space-orientation RFs that are uniform, nonuniform, and nonuniform with bimodal orientation tuning, respectively. Hatched circles, RFs of V1 subunits. Solid and dashed circles, classical RF of the subunit and inhibitory surround of the classical RF, respectively; orientation of the hatches, preferred orientation for the classical RF and the most suppressive orientation for the surround. Black and gray circles, RF locations in space; RFs in the same shade occupy a common region of visual space. Small open and filled circles, excitatory and inhibitory synapses, respectively. (**a**) Excitation models. (**b**) Inhibition models. (**c**) Disinhibition models.

orientation selectivity similar to that of an orientation-selective V1 neuron. When the optimal combination is a particular pair of dissimilar orientations, the neuron would be excited by certain angles and curves and may be inhibited by uniform orientations. This may explain why some V2 neurons respond to complex stimuli[10–12,18] despite the lack of neurons showing more than one peak in orientation tuning when tested with large gratings[8] or bars[9].

The visual system integrates collinear line segments to achieve contour perception[19–21]. V2 neurons that encode combinations of collinear orientations may have a part in this process. On the other hand, noncollinear orientation combinations are useful cues for surface segmentation. For example, L and T junctions are necessary for perceiving amodal surface completion and illusory contours[22]. V2 neurons that convey signals about these junctions may initiate a contour completion process[22] that may in turn spread among neurons encoding collinear orientations to enclose surfaces. V2 neurons that encode combinations of local orientations may thus provide important underpinnings for the analysis of surfaces[23] and ultimately object recognition[24].

Our results suggest the following picture for mechanisms that may underlie RFs of orientation-selective V2 neurons. First of all, interactions described by TSIs around 1 (**Fig. 5c,d**) suggest that some V2 neurons combine orientation-selective V1 inputs additively (**Fig. 7a**). If V1 subunits shared the same orientation preference, the space-orientation RFs of these V2 neurons would be uniform (**Fig. 7a**, left), whereas the RFs would be nonuniform if the subunits were tuned to different orientations (**Fig. 7a**, right). The output nonlinearity of V2 neurons is assumed to be a half-rectification in these models. If, instead, the nonlinearity takes an expansive form, the models predict an amplitude reduction of orientation tuning for orthogonal conditioning, and moderate TSI values (**Figs. 3h–j** and **4d–f**). Although the amplitude reduction could be accounted for by divisive nonlinearity (for example, response normalization[25]) or orientation-tuned inhibition, such mechanisms involve more complicated circuitries than the models depicted here.

Models of neurons that show flat tuning for orthogonal conditioning (**Fig. 5g,h**) must incorporate an inhibitory mechanism (**Fig. 7b**). The inhibition might be of V2 intracortical origin (**Fig. 7b**, top), such as mutual inhibition between V2 neurons tuned to orthogonal orientations at a given location in the RF (orientation domain push-pull), or of V1 intracortical origin (**Fig. 7b**, bottom), such as a combination of end[5,26] and side[26,27] inhibition[28] arranged in a spatially complementary manner (the classical RF of the end-inhibitory neuron overlaps with the surround of the side-inhibitory neuron and vice versa).

Finally, to account for the disinhibitory effect manifested by tuning shape inversion (**Fig. 5k,l**), we propose models that consist of a pair of either end- or side-inhibitory V1 neurons[29] that are spatially complementary (**Fig. 7c**, left). As a special case, the double end– and double side–inhibition models are combined (**Fig. 7c**, right) so that the space-orientation RF shows bimodal tuning.

Our suggestion that end- and/or side-inhibitory V1 neurons are likely to be involved in construction of some V2 RFs is based on our observation that the tuning shown in **Figure 5k,l** is unimodal, whereas single-patch tuning curves (**Fig. 5j**) are bimodal. This indicates that the inhibition was acting on one peak: that is, the inhibition must have taken place before the convergence of excitatory inputs tuned to different orientations. End-inhibitory V1 neurons have been implicated for curvature processing[5,30]. We take this notion one step further by proposing that V2 neurons encode combinations of orientations using end- and/or side-inhibitory V1 inputs.

Finally, the architecture laid out here for encoding combinations of orientations can be easily extended to other visual attributes such as motion, binocular disparity and spatial frequency to create neurons that signal combinations of two inputs. For instance, adding direction selectivity to V1 subunits of end- and side-inhibition models (**Fig. 7b,c**) would yield V2 neurons that respond to pattern motion, which could provide an intermediate computational stage for the recent model of pattern motion–selective MT neurons[31].

METHODS

General procedures. We used sixteen monkeys (*Macaca fascicularis*). All surgical and experimental procedures complied with the guidelines set by the US National Institutes of Health and were approved by Animal Studies Committee at Washington University School of Medicine. The animal was under anesthesia (propofol 2–4.5 mg h^{-1} per kilogram body weight plus sufentanil citrate 4–36 μg kg^{-1} h^{-1}) and was positioned on a stereotaxic frame during the entire procedure. In an aseptic condition, we made a craniotomy of about 1.5 cm long and 1 cm wide approximately 2 cm anterior to the occipital bone ridge and 7 mm lateral from the midline. Duratomies of 1–2 mm in diameter were made just posterior to the lunate sulcus. We mounted a recording chamber over the craniotomy, filled with mineral oil and sealed to minimize cerebral pulsation. The animal was paralyzed (gallamine triethiodide, 10 mg kg^{-1} h^{-1}) before recording sessions began. Oxygen-permeable contact lenses were placed on both corneas, and eyes were refracted and corrected with additional lenses. Pupils were dilated, and an artificial pupil placed in front of each eye.

We inserted an epoxy-coated tungsten electrode (A-M Systems) into the cortex through the duratomy, and attempted extracellular recordings on single units in the visual area V2. The electrode traveled from the superficial cortex near the V1/V2 border, down through the posterior bank of the lunate sulcus at the angles of about 5–25° anterior and 5–20° medial. Occasionally, the electrode would enter the V1 side of the V1-V2 border or reach V3 after a long penetration, in which case we collected data from some cells in these

areas. At the end of each penetration, we made lesions (7 μA, 7 s) along the recording track.

At the conclusion of the physiological experiment, we injected an overdose of pentobarbital sodium (60 mg kg^{-1}) intravenously, perfused intracardially with 0.1 M PO_4 buffer followed by 4% paraformaldehyde, and removed the brain from the skull. The brain tissue was sectioned on a microtome at 50-μm intervals in a direction perpendicular to the V1/V2 border (that is, parasagittally) and roughly parallel to the recording tracks so that the V1/V2 border and recording tracks were easily identifiable on the sectioned tissues, which were processed for Nissl staining, cytochrome oxidase staining or CAT-301 antibody reaction. To identify locations of recording tracks, we used Photoshop (Adobe) to superimpose and manually align digital images of the tissue sections. The cortical areas along the recording tracks were identified based on histological landmarks, physiological records of RF size, location in the visual field, and topographical progression along the tracks. As the angle of tissue sectioning was parallel to cytochrome oxidase stripe patterns in V2, we were unable to identify cytochrome oxidase stripes from which recordings were made.

Electrophysiological recording. Visual stimuli were presented on a computer monitor (mean luminance 24 cd m^{-2}) placed 114 cm in front of the animal. An electrode signal was recorded during stimulus presentations using Spike2 on Power 1401 (Cambridge Electronic Design) at a sampling rate of 25 kHz, and the entire signal, including spike and interspike waveforms, was stored on a computer hard disk.

We measured tuning for orientation and spatial frequency with drifting sinusoidal gratings that covered the entire extent of the cell's classical RF, and estimated preferred orientation and spatial frequency for each cell. Then we measured orientation tuning at various positions within the classical RF using small circular, stationary sinusoidal gratings of about one-quarter to one-third the RF diameter. The stimuli were presented in rapid sequences of 40 ms each at one of 19 locations arranged in a hexagonal array over an area slightly bigger than the classical RF and at one of 13 orientations equally spaced between 0° and 180° (13.85° interval). The location and orientation of the gratings were randomized. The stimulus sequence was rerandomized and repeated 50–100 times. The spatial frequency of the gratings was set to that preferred, or slightly higher than that preferred, for each cell so that the gratings contained a minimum of 1.2 cycles (the majority of recordings were made with 1.2 cycle gratings; the maximum used was 3.6 cycles). The spatial phase of the gratings was fixed at 90° (that is, even symmetric). For circular gratings containing 1.2 cycles at an even symmetric spatial phase, the mean luminance of the gratings was equal to the background luminance. The orientation bandwidth of the stimuli was approximately 45° (the full-width at half-height of the main lobe of the stimulus Fourier spectrum, which is a sinc function) for 1.2-cycle gratings, and it decreased with the stimulus cycle (for example, 27° for 2 cycles).

For a subset of cells, upon completion of the orientation tuning measurement we examined orientation interactions between two positions within the classical RF. Based on the responsiveness and preferred orientation at each location in the orientation tuning just obtained, we chose up to four positions of interest. Then we presented pairs of sinusoidal gratings in rapid sequences at various combinations of orientations and positions. The gratings had the same size, spatial frequency and phase as those used in the orientation tuning measurement, but their orientations were reduced to six variations at 30° intervals to minimize the total number of conditions and still maintain a reasonable resolution for the measurement. The orientation and position combinations were randomly selected without replacement from the list of all possible combinations. As a control, we also inserted single gratings randomly into the stimulus sequence to measure orientation tuning for individual positions. Otherwise, the stimuli were presented in the same manner as that for the orientation tuning measurements.

Data analysis. *Spike sorting.* A nonuniform RF could result if the electrode signal reflected the activity of multiple units tuned to different orientations. To ensure that we were obtaining RFs from single-unit activities, we sorted spikes off-line based on their shapes, using a template-matching functionality of Spike2. An amplitude threshold was set for each recording at a level between 3 and 4 s.d. from the mean of the signal amplitude distribution. The signal waveform within a 1–2 ms interval around the point where the waveform crossed the threshold was considered a spike and classified according to its shape. We excluded units with fewer than 1,000 spikes from our analysis. The Spike2 template-matching process typically yielded a few units with distinct but often similar spike shapes. As there was no way of knowing whether small differences in spike shape reflected true differences among units or variations among spikes of a single unit, we chose the one unit with the most spikes (median spike counts 4,814, maximum 38,080) from each recording to be included in our sample for RF analyses. On a few occasions, the spike shape of another unit was unequivocally different from that of the first unit, and the second unit was added to the sample as well.

Cell classification. To ensure recording stability, the duration of each test run was kept under 20 min. To obtain well defined orientation tuning curves with up to 100 repetitions per orientation under this constraint, we limited the number of stimulus conditions by fixing the stimulus spatial phase. This is not a problem for complex cells whose responses are independent of the stimulus spatial phase. However, for simple cells, orientation tuning depends on stimulus spatial phase, and fixing the phase could result in erroneous tuning. For this reason, we recorded primarily from complex cells, and cells that were later determined to be simple cells were excluded from our analyses. We classified cells as simple cells based on Fourier analysis if the ratio of the power in the first-harmonic response to drifting sinusoidal gratings summed over all stimulus conditions to that in the steady-state (DC) response exceeded 0.6. This criterion is less stringent than those previously proposed[32] so that we classified borderline cells with weak but significant sensitivity to spatial phase as simple cells. For the remaining cells classified as complex cells, we found no obvious dependence of RF structure on the first harmonic to DC response ratios.

Constructing space-orientation RFs and orientation interaction maps. We cross-correlated the spike train recorded during the stimulus presentation with the stimulus sequence to obtain a map of responses relative to the baseline response (the mean firing rate of the spike train) at a correlation delay that yielded the maximum response power. For orientation tuning measurements, the map is a function of stimulus position and orientation, which we call a 'space-orientation RF'. For orientation interaction measurements, the map is a function of stimulus orientations at two positions between which interactions were examined. We call this map an 'orientation interaction map'.

Estimating preferred orientations. To obtain the preferred orientation for each location in the space-orientation RF map, we first determined locations where orientation tuning had significant signals by computing an S/N (the ratio of the response power averaged over all stimulus conditions to the power of the baseline response) for each location. Then, for each location with an S/N greater than 2, we performed a modality test on the orientation tuning to estimate the number of modes in the tuning. The test was based on a kernel density estimate method[13,33] with a von Mises function (the circular analog of the normal distribution; see ref. 14) as a kernel, and Watson's U^2 statistic[34] corrected for grouping[35] was computed as a goodness-of-fit test statistic to obtain a P value through a bootstrapping procedure[36]. For unimodal tuning curves, we fitted a von Mises function of the form

$$R = a \cdot \exp[k\{\cos(2(\theta - \theta_0)) - 1\}] + b \quad (1)$$

to the data to obtain the preferred orientation θ_0, where R and θ represent the response and the stimulus orientation, respectively, and a, k, θ_0, and b are the parameters to be fitted and denote amplitude, concentration, center orientation and baseline response, respectively. For bimodal tuning curves, we used a sum of two von Mises functions described by

$$R = a_1 \cdot \exp[k_1\{\cos(2(\theta - \theta_1)) - 1\}] + a_2 \cdot \exp\,[k_2\{\cos(2(\theta - \theta_2)) - 1\}] + b \quad (2)$$

to fit the data, where a_i, k_i, and θ_i ($i = 1,2$) denote amplitude, concentration and center (preferred) orientation of the tuning curve associated with the ith mode, respectively; other variables are the same as defined in equation (1). Fitting was performed in Matlab (Mathworks) using a nonlinear least-squares minimization function lsqnonlin(), and the jacobian returned by the function was used to compute standard errors for the best fit parameters[37]. We considered fits that yielded preferred orientations with standard errors greater than 9° (5% of the maximum possible error of 180°) poor, and excluded them

from the analysis of the preferred orientation. This eliminated fits in the upper fifth percentile of the standard error distribution as outliers.

ACKNOWLEDGMENTS

We thank D. Marcus and J. Hegde for their participation in data collection and S. Kumar, E. Reid, M. K. Harmon, and C. Faulkner for their assistance with experiments. We are grateful to E. Kaplan for his advice on propofol, to S. Marron for information on mode testing and to G. DeAngelis for his comments and suggestions on the manuscript. This work was supported by a grant from the US National Eye Institute (EY 02091).

AUTHOR CONTRIBUTIONS

A.A. conceived the project, designed and performed the experiments and wrote the manuscript; X.P. performed the experiments; D.C.V. supervised and contributed in all phases of the project including data collection.

Published online at http://www.nature.com/natureneuroscience
Reprints and permissions information is available online at http://npg.nature.com/reprintsandpermissions

1. Hubel, D.H. & Wiesel, T.N. Receptive fields of single neurones in the cat's striate cortex. *J. Physiol. (Lond.)* **148**, 574–591 (1959).
2. Hubel, D.H. & Wiesel, T.N. Receptive fields and functional architecture of monkey striate cortex. *J. Physiol. (Lond.)* **195**, 215–243 (1968).
3. Kuypers, H.G., Szwarcbart, M.K., Mishkin, M. & Rosvold, H.E. Occipitotemporal corticocortical connections in the rhesus monkey. *Exp. Neurol.* **11**, 245–262 (1965).
4. Van Essen, D.C., Newsome, W.T., Maunsell, J.H. & Bixby, J.L. The projections from striate cortex (V1) to areas V2 and V3 in the macaque monkey: asymmetries, areal boundaries, and patchy connections. *J. Comp. Neurol.* **244**, 451–480 (1986).
5. Hubel, D.H. & Wiesel, T.N. Receptive fields and functional architecture in two nonstriate visual areas (18 and 19) of the cat. *J. Neurophysiol.* **28**, 229–289 (1965).
6. Hubel, D.H. & Wiesel, T.N. Stereoscopic vision in macaque monkey. Cells sensitive to binocular depth in area 18 of the macaque monkey cortex. *Nature* **225**, 41–42 (1970).
7. Smith, A.T., Singh, K.D., Williams, A.L. & Greenlee, M.W. Estimating receptive field size from fMRI data in human striate and extrastriate visual cortex. *Cereb. Cortex* **11**, 1182–1190 (2001).
8. Levitt, J.B., Kiper, D.C. & Movshon, J.A. Receptive fields and functional architecture of macaque V2. *J. Neurophysiol.* **71**, 2517–2542 (1994).
9. Hubel, D.H. & Livingstone, M.S. Segregation of form, color, and stereopsis in primate area 18. *J. Neurosci.* **7**, 3378–3415 (1987).
10. Hegde, J. & Van Essen, D.C. Selectivity for complex shapes in primate visual area V2. *J. Neurosci.* **20**, RC61 (2000).
11. Mahon, L.E. & De Valois, R.L. Cartesian and non-Cartesian responses in LGN, V1, and V2 cells. *Vis. Neurosci.* **18**, 973–981 (2001).
12. Ito, M. & Komatsu, H. Representation of angles embedded within contour stimuli in area V2 of macaque monkeys. *J. Neurosci.* **24**, 3313–3324 (2004).
13. Fisher, N.I. & Marron, J.S. Mode testing via the excess mass estimate. *Biometrika* **88**, 499–517 (2001).
14. Fisher, N.I. *Statistical Analysis of Circular Data* (Cambridge Univ Press, New York, 1993).
15. Berry, D.A. *Statistics: A Bayesian Perspective* (Duxbury, Belmont, California, 1996).
16. Heeger, D.J. Half-squaring in responses of cat striate cells. *Vis. Neurosci.* **9**, 427–443 (1992).
17. DeAngelis, G.C., Ohzawa, I. & Freeman, R.D. Neuronal mechanisms underlying stereopsis: how do simple cells in the visual cortex encode binocular disparity? *Perception* **24**, 3–31 (1995).
18. Kobatake, E. & Tanaka, K. Neuronal selectivities to complex object features in the ventral visual pathway of the macaque cerebral cortex. *J. Neurophysiol.* **71**, 856–867 (1994).
19. Polat, U. & Sagi, D. Lateral interactions between spatial channels: suppression and facilitation revealed by lateral masking experiments. *Vision Res.* **33**, 993–999 (1993).
20. Polat, U. & Sagi, D. The architecture of perceptual spatial interactions. *Vision Res.* **34**, 73–78 (1994).
21. Field, D.J., Hayes, A. & Hess, R.F. Contour integration by the human visual system: evidence for a local "association field". *Vision Res.* **33**, 173–193 (1993).
22. Rubin, N. The role of junctions in surface completion and contour matching. *Perception* **30**, 339–366 (2001).
23. Nakayama, K., He, Z.J. & Shimojo, S. Visual surface representation: a critical link between lower-level and higher-level vision. in *An Invitation to Cognitive Science* Vol. 2 (eds. Kosslyn, S. & Osherson, D.N.) 1–70 (MIT Press, Cambridge, Massachusetts, 1995).
24. Riesenhuber, M. & Poggio, T. Hierarchical models of object recognition in cortex. *Nat. Neurosci.* **2**, 1019–1025 (1999).
25. Carandini, M., Heeger, D.J. & Movshon, J.A. Linearity and normalization in simple cells of the macaque primary visual cortex. *J. Neurosci.* **17**, 8621–8644 (1997).
26. Maffei, L. & Fiorentini, A. The unresponsive regions of visual cortical receptive fields. *Vision Res.* **16**, 1131–1139 (1976).
27. De Valois, R.L., Thorell, L.G. & Albrecht, D.G. Periodicity of striate-cortex-cell receptive fields. *J. Opt. Soc. Am. A* **2**, 1115–1123 (1985).
28. DeAngelis, G.C., Freeman, R.D. & Ohzawa, I. Length and width tuning of neurons in the cat's primary visual cortex. *J. Neurophysiol.* **71**, 347–374 (1994).
29. Walker, G.A., Ohzawa, I. & Freeman, R.D. Disinhibition outside receptive fields in the visual cortex. *J. Neurosci.* **22**, 5659–5668 (2002).
30. Dobbins, A., Zucker, S.W. & Cynader, M.S. Endstopped neurons in the visual cortex as a substrate for calculating curvature. *Nature* **329**, 438–441 (1987).
31. Rust, N.C., Mante, V., Simoncelli, E.P. & Movshon, J.A. How MT cells analyze the motion of visual patterns. *Nat. Neurosci.* **9**, 1421–1431 (2006).
32. Skottun, B.C. *et al.* Classifying simple and complex cells on the basis of response modulation. *Vision Res.* **31**, 1079–1086 (1991).
33. Silverman, B.W. Using kernel density estimates to investigate multimodality. *J. R. Stat. Soc. Ser B Methodol.* **43**, 97–99 (1981).
34. Watson, G.S. Goodness-of-fit tests on a circle. *Biometrika* **48**, 109–114 (1961).
35. Brown, B.M. Grouping corrections for circular goodness-of-fit tests. *J. R. Stat. Soc. Ser B Methodol.* **56**, 275–283 (1994).
36. Efron, B. Bootstrap methods: another look at the jackknife. *Ann. Stat.* **7**, 1–26 (1979).
37. Press, W.H., Flannery, B.P., Teukolsky, S.A. & Vetterling, W.T. Modeling of data. *Numerical Recipes in C: The Art of Scientific Computing* 517–565 (Cambridge Univ. Press, New York, 1988).